Title
Real-time simultaneous single snapshot of optical properties and blood flow using coherent spatial frequency domain imaging (cSFDI)

Permalink
https://escholarship.org/uc/item/6d257951

Journal
Biomedical Optics Express, 7(3)

ISSN
2156-7085

Authors
Ghijsen, Michael
Choi, Bernard
Durkin, Anthony J
et al.

Publication Date
2016-03-01

DOI
10.1364/boe.7.000870

Peer reviewed

Real-time simultaneous single snapshot of optical properties and blood flow using coherent spatial frequency domain imaging (cSFDI)

Michael Ghijsen,[1,2] Bernard Choi,[1,2,3] Anthony J. Durkin,[1,3] Sylvain Gioux,[4] and Bruce J. Tromberg[1,2,3,*]

[1]*Laser Microbeam and Medical Program, Beckman Laser Institute, 1002 Health Sciences Road, Irvine, California 92612, USA*
[2]*Department of Biomedical Engineering, University of California, Irvine, California 92697, USA*
[3]*Department of Surgery, University of California, Irvine Medical Center, Orange, California 92868, USA*
[4]*University of Strasbourg, ICube Laboratory, 300 Bd S. Brant, 67412 Illkirch, France*
*bjtrombe@uci.edu

Abstract: In this work we present and validate a wide-field method for the real-time mapping of tissue absorption, scattering and blood flow properties over wide regions of tissue (15 cm x 15 cm) with high temporal resolution (50 frames per second). We achieve this by applying Fourier Domain demodulation techniques to coherent spatial frequency domain imaging to extract optical properties and speckle flow index from a single snapshot. Applying this technique to forearm reactive hyperemia protocols demonstrates the ability to resolve intrinsic physiological signals such as the heart beat waveform and the buildup of deoxyhemoglobin associated with oxygen consumption.

References and links

1. D. Ratner, C. O. Thomas, and D. Bickers, "The uses of digital photography in dermatology," J. Am. Acad. Dermatol. **41**(5), 749–756 (1999).
2. B. J. Tromberg, O. Coquoz, J. B. Fishkin, T. Pham, E. R. Anderson, J. Butler, M. Cahn, J. D. Gross, V. Venugopalan, and D. Pham, "Non-invasive measurements of breast tissue optical properties using frequency-domain photon migration," Philos. Trans. R. Soc. Lond. B Biol. Sci. **352**(1354), 661–668 (1997).
3. D. J. Cuccia, F. Bevilacqua, A. J. Durkin, and B. J. Tromberg, "Modulated imaging: quantitative analysis and tomography of turbid media in the spatial-frequency domain," Opt. Lett. **30**(11), 1354–1356 (2005).
4. J. D. Briers, "Laser Doppler and time-varying speckle: a reconciliation," J. Opt. Soc. Am. A **13**(2), 345–350 (1996).
5. A. Mazhar, D. J. Cuccia, T. B. Rice, S. A. Carp, A. J. Durkin, D. A. Boas, B. Choi, and B. J. Tromberg, "Laser speckle imaging in the spatial frequency domain," Biomed. Opt. Express **2**(6), 1553–1563 (2011).
6. T. B. Rice, S. D. Konecky, A. Mazhar, D. J. Cuccia, A. J. Durkin, B. Choi, and B. J. Tromberg, "Quantitative determination of dynamical properties using coherent spatial frequency domain imaging," J. Opt. Soc. Am. A **28**(10), 2108–2114 (2011).
7. T. B. Rice, S. D. Konecky, C. Owen, B. Choi, and B. J. Tromberg, "Determination of the effect of source intensity profile on speckle contrast using coherent spatial frequency domain imaging," Biomed. Opt. Express **3**(6), 1340–1349 (2012).
8. M. A. Davis, S. M. Kazmi, and A. K. Dunn, "Imaging depth and multiple scattering in laser speckle contrast imaging," J. Biomed. Opt. **19**(8), 086001 (2014).
9. A. Fercher and J. Briers, "Flow visualization by means of single-exposure speckle photography," Opt. Commun. **37**(5), 326–330 (1981).
10. J. D. Briers and S. Webster, "Laser speckle contrast analysis (LASCA): a nonscanning, full-field technique for monitoring capillary blood flow," J. Biomed. Opt. **1**(2), 174–179 (1996).
11. B. Choi, N. M. Kang, and J. S. Nelson, "Laser speckle imaging for monitoring blood flow dynamics in the in vivo rodent dorsal skin fold model," Microvasc. Res. **68**(2), 143–146 (2004).
12. A. K. Dunn, H. Bolay, M. A. Moskowitz, and D. A. Boas, "Dynamic imaging of cerebral blood flow using laser speckle," J. Cereb. Blood Flow Metab. **21**(3), 195–201 (2001).

13. D. D. Duncan and S. J. Kirkpatrick, "Can laser speckle flowmetry be made a quantitative tool?" J. Opt. Soc. Am. A **25**(8), 2088–2094 (2008).
14. D. J. Cuccia, F. Bevilacqua, A. J. Durkin, F. R. Ayers, and B. J. Tromberg, "Quantitation and mapping of tissue optical properties using modulated imaging," J. Biomed. Opt. **14**, 024012 (2009).
15. A. Corlu, T. Durduran, R. Choe, M. Schweiger, E. M. Hillman, S. R. Arridge, and A. G. Yodh, "Uniqueness and wavelength optimization in continuous-wave multispectral diffuse optical tomography," Opt. Lett. **28**(23), 2339–2341 (2003).
16. A. Mazhar, S. Dell, D. J. Cuccia, S. Gioux, A. J. Durkin, J. V. Frangioni, and B. J. Tromberg, "Wavelength optimization for rapid chromophore mapping using spatial frequency domain imaging," J. Biomed. Opt. **15**, 061716 (2010).
17. S. D. Konecky, T. Rice, A. J. Durkin, and B. J. Tromberg, "Imaging scattering orientation with spatial frequency domain imaging," J. Biomed. Opt. **16**(12), 126001 (2011).
18. B. Weber, C. Burger, M. T. Wyss, G. K. von Schulthess, F. Scheffold, and A. Buck, "Optical imaging of the spatiotemporal dynamics of cerebral blood flow and oxidative metabolism in the rat barrel cortex," Eur. J. Neurosci. **20**(10), 2664–2670 (2004).
19. T. Hamaoka, H. Iwane, T. Shimomitsu, T. Katsumura, N. Murase, S. Nishio, T. Osada, Y. Kurosawa, and B. Chance, "Noninvasive measures of oxidative metabolism on working human muscles by near-infrared spectroscopy," J. Appl. Physiol. **81**(3), 1410–1417 (1996).
20. K. P. Nadeau, A. J. Durkin, and B. J. Tromberg, "Advanced demodulation technique for the extraction of tissue optical properties and structural orientation contrast in the spatial frequency domain," J. Biomed. Opt. **19**(5), 056013 (2014).
21. J. Vervandier and S. Gioux, "Single snapshot imaging of optical properties," Biomed. Opt. Express **4**(12), 2938–2944 (2013).
22. M. van de Giessen, J. P. Angelo, and S. Gioux, "Real-time, profile-corrected single snapshot imaging of optical properties," Biomed. Opt. Express **6**(10), 4051–4062 (2015).
23. J. C. Ramirez-San-Juan, R. Ramos-García, I. Guizar-Iturbide, G. Martínez-Niconoff, and B. Choi, "Impact of velocity distribution assumption on simplified laser speckle imaging equation," Opt. Express **16**(5), 3197–3203 (2008).
24. F. Ayers, A. Grant, D. Kuo, D. J. Cuccia, and A. J. Durkin, "Fabrication and characterization of silicone-based tissue phantoms with tunable optical properties in the visible and near infrared domain," in *Biomedical Optics (BiOS) 2008*(International Society for Optics and Photonics2008), pp. 687007.
25. B. Choi, J. C. Ramirez-San-Juan, J. Lotfi, and J. S. Nelson, "Linear response range characterization and in vivo application of laser speckle imaging of blood flow dynamics," J. Biomed. Opt. **11**, 041129 (2006).
26. M. Eliakim, D. Sapoznikov, and J. Weinman, "Pulse wave velocity in healthy subjects and in patients with various disease states," Am. Heart J. **82**(4), 448–457 (1971).
27. B. P. Imholz, W. Wieling, G. A. van Montfrans, and K. H. Wesseling, "Fifteen years experience with finger arterial pressure monitoring: assessment of the technology," Cardiovasc. Res. **38**(3), 605–616 (1998).

Introduction

Cameras are used ubiquitously throughout medicine as a simple noncontact approach to illustrate and document diseases. In dermatology for example, color photography captures details of skin pathology to relay information to physicians working from a remote location and is capable of monitoring disease progression over time [1]. Although useful in numerous applications, digital photography is only able to relay qualitative information. Cameras are able to capture superficial structural details of the underlying disease, but are unable to retrieve quantitative information such as the absolute concentrations of tissue biochemical constituents. Improved quantitative accuracy would make the technique a more powerful means of diagnosis, disease staging and therapeutic monitoring.

One approach to improving quantitative accuracy of cameras is to manipulate the illumination characteristics of the light source. These manipulations can consist of modulating the source intensity in space or time, controlling the source coherence, and selective choice of the source wavelength [2–4]. Coherent spatial frequency domain imaging (cSFDI) utilizes spatially modulated coherent light to characterize tissue absorption and scattering characteristics over scalable fields-of-view [5–7]. cSFDI is essentially Laser Speckle Imaging (LSI) performed in the spatial frequency domain (SFD). LSI is a technique that uses coherent light to measure blood flow in superficial microcirculation by measuring the dynamic speckle interference pattern resulting from interactions occurring between the incident light and moving red blood cells, and extrapolating this to a metric referred to as the speckle flow index (SFI) [8–11]. Although LSI is capable of rapid measurements over large spatial regions, the

data lack quantitative accuracy and are limited to detecting relative changes in blood flow [12]. One reason for this is the confounding effect of spatial and temporal variations in the tissue absorption and reduced scattering coefficients (μ_a and μ_s', respectively) on SFI [13].

cSFDI can decouple μ_a and μ_s' with the use of Spatial Frequency Domain (SFD) techniques, and then potentially use this information to correct for errors imparted on SFI. These SFD methods, which we have previously described in detail [3, 14], employ structured coherent illumination. Images of back-scattered reflectance are then acquired at multiple spatial frequencies using a CCD or CMOS detector. Computational models of photon transport are then applied to the measurements to extract μ_a and μ_s' from diffuse reflectance images acquired at multiple spatial frequencies. By acquiring μ_a at multiple optical wavelengths, the Beer-Lambert law can be invoked to recover the concentration of tissue chromophores such as oxyhemoglobin, deoxyhemoglobin, water and lipid [15, 16]. In addition μ_s' can reveal information pertaining to tissue structure and orientation [17]. The combination of these parameters allows for the assessment of the relative metabolic rate of oxygen consumption in accordance with Fick's Principle [18, 19].

Conventional cSFDI techniques require large volumes of raw data, limiting the rate at which μ_a, μ_s', and SFI can be recovered. This is due to the number of raw images needed to quantitatively characterize the light-tissue interactions [20]. Recently, signal processing techniques have been applied to SFD methods to demodulate data with fewer raw images [20, 21]. One method introduced by Vervandier et al. is capable of extracting tissue optical properties from a single snapshot of raw data, reducing the number of raw images by a factor of 6 [21, 22]. This technique applies spatial Discrete Fourier Transforms, followed by frequency domain processing to demodulate two spatial frequencies from a single frame of raw data. In comparison with conventional demodulation methods, this approach – referred to as Single Snapshot of Optical Properties (SSOP) – reduces the number of frames by a factor of 6 allowing for real-time mapping of optical properties. In addition to reducing the amount of raw data, SSOP allows for the use of static objects as a spatial light modulator since only a single pattern is needed to recover optical properties. This is in contrast to conventional demodulation approaches which require multiple patterns demanding the use of computer controlled spatial light modulators such as a digital micromirror device (DMD) or liquid crystal on silicon (LCOS) chips. In short, the ability to extract all the necessary information from a single image allows for real-time property acquisition and simplified, cost-effective instrumentation.

In this work we introduce and validate the application of SSOP demodulation to cSFDI in order to extract optical properties and speckle contrast from a single snapshot. We present the algorithmic implementation of SSOP demonstrating the steps required to extract μ_a, μ_s', and SFI from a single image of spatially modulated coherent light. In addition, we introduce a simple cSFDI instrument build that requires only one sinusoidal-patterned slide to achieve spatial light modulation. Next, in two *in vitro* experiments we present data validating single snapshot cSFDI in comparison with conventional techniques. In the first set of experiments we use homogeneous phantoms to demonstrate our ability to accurately recover bulk optical properties. In the second validation experiment we use a flow-phantom to compare single snapshot cSFDI with conventional LSI in terms of sensitivity to changes in flow speed. Finally, we report on *in vivo* experiments on a human forearm undergoing post-occlusive reactive hyperemia via a cuff-occlusion-release protocol. The *in vivo* data demonstrate sensitivity to intrinsic physiological signals such as the accumulation of deoxyhemoglobin in occluded tissue and heartbeat fluctuations observed from SFI values. Although optical property correction can be performed on flow measurements, this computational step is left to future studies.

Materials and methods

Single snapshot cSFDI instrument setup (Fig. 1)

A 120 mW 660 nm laser diode (HL6545MG Opnext Inc.) was powered and stabilized using a combined laser diode and temperature controller (Newport Corporation). Coherent light from the laser diode was spatially homogenized using a ground glass diffuser and then condensed onto a sinusoidal-patterned slide (Applied Image Inc.). The pattern was imaged onto the sample using an objective lens in off-axis configuration. The sinusoidal projection pattern had a fixed spatial frequency of 0.185 mm^{-1}. Data was recorded using a high-speed sCMOS camera (Hamamatsu Photonics, Orca Flash 4.0) with a cross polarizer placed in front of a 16 mm fixed focal length lens (Edmund Optics). For all experiments mentioned below, the lens aperture was f/5.6 and the integration time was 20 ms, allowing for a data acquisition rate of 50 frames per second. The aperture and integration time were set to manage the trade-off in accuracy between speckle contrast and optical properties (Fig. 1).
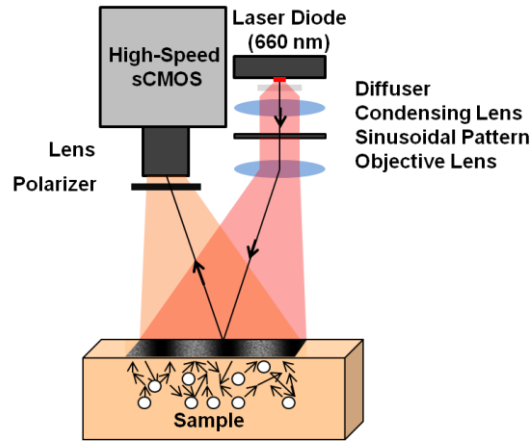

Fig. 1. Experimental setup. Light from a coherent source is spatially modulated and projected onto a diffuse medium. Remitted light from the sample is collected using a high-speed sCMOS camera.

Three-phase demodulation from conventional SFDI

Conventional SFDI and cSFDI utilize an algebraic demodulation technique referred to as the three-phase method. This method recovers AC intensity from three frames with relative modulation phases of 0, 120, and 240 degrees. A simple algebraic formula (Eq. (1)) is applied to these phase-offset images to extract pixel-by-pixel AC information content. It should be noted that only a single spatial frequency is demodulated at a time from these three phases.

$$AC(x, y) = \sqrt{[I_{0°} - I_{120°}]^2 + [I_{120°} - I_{240°}]^2 + [I_{240°} - I_{0°}]^2} \qquad (1)$$

Single snapshot cSFDI data processing (Fig. 2)

A single raw image is used to simultaneously extract μ_a, μ_s', and SFI. In order to calculate μ_a and μ_s', a Fourier transform is applied line by line to raw data to calculate the spatial frequency spectrum of each column vector. This frequency domain data is subdivided into the DC and AC component spectra using top-hat window functions. The cutoff frequency of the window functions was set to 0.11 mm^{-1}, and was selected to optimize demodulated image quality specific to our selected spatial frequency. The DC and AC demodulated images are then computed by performing line-by-line inverse Fourier transforms (Fig. 2). The process of converting raw data to demodulated DC and AC data is more fully described in Vervandier et al. [21] The data is calibrated using a phantom with known optical properties to calculate the

calibrated diffuse reflectance (step not pictured). The calibration process is outlined extensively in Cuccia et al. [3, 14]. Finally, optical properties are recovered pixel-by-pixel from the DC and AC diffuse reflectance using a Levenberg-Marquardt fit of experimental data to a light-transport model data based on Monte Carlo simulations or the photon diffusion equation [14].

The speckle flow index (SFI) is calculated from the same raw image. Similar to conventional LSI approaches, a 7 pixel x 7 pixel sliding window filter is used to calculate the local spatial standard deviation σ (I) and mean intensity $\langle I \rangle$. The ratio of these two components is the speckle contrast (K). Finally, the SFI is calculated pixel-by-pixel according to the equation $SFI = 1/(2TK^2)$ where T is the integration time and K is the speckle contrast [23]. SFI is a non-quantitative measurement used as a proxy for relative flow [23].

Homogeneous phantom experiments

Homogeneous phantoms were used to validate the ability of single snapshot cSFDI to estimate bulk optical properties by demonstrating agreement with conventional SFDI. Seven silicone phantoms with unique optical properties were constructed according to Ayers et al. [24]. The μ_a of these phantoms ranged from 0.01 to 0.05 mm^{-1} while μ_s' ranged from 0.5 to 1.5 mm^{-1}. Recovered bulk optical properties were calculated using single snapshot cSFDI and the standard three-phase SFDI technique. μ_a and μ_s' were determined by averaging over a 10 cm x 10 cm region over the center of each phantom. The phantom properties were chosen to demonstrate agreement between single snapshot cSFDI and conventional SFDI. The accuracy, linearity and agreement between SFDI and single snapshot SFDI has already been established over a wide range of optical properties [14, 21]. Due to the non-trivial nature of the phantom making process, the optical properties are not equally spaced.
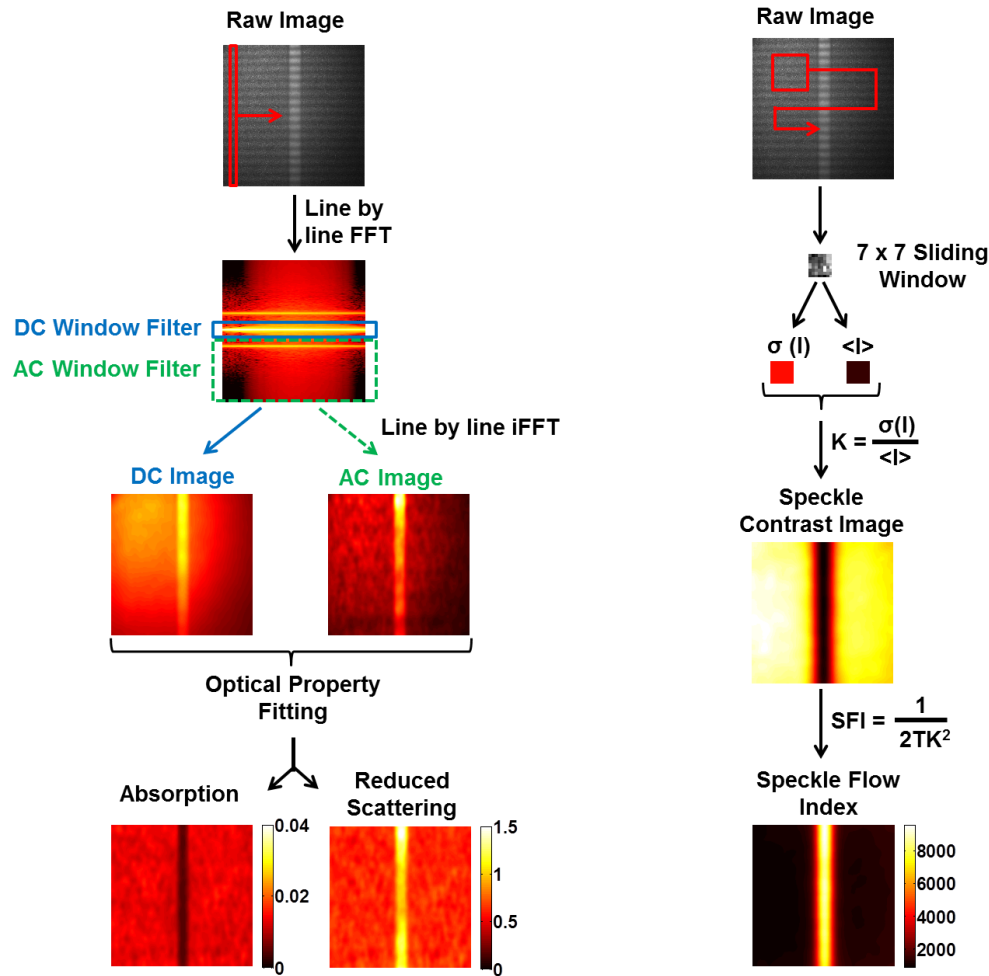
Raw Image

Line by line FFT

DC Window Filter

AC Window Filter

Line by line iFFT

DC Image   **AC Image**

Optical Property Fitting

Absorption   **Reduced Scattering**

0.04
0.02
0

1.5
1
0.5
0

Raw Image

7 x 7 Sliding Window

$\sigma(I)$ $<I>$

$K = \dfrac{\sigma(I)}{<I>}$

Speckle Contrast Image

$SFI = \dfrac{1}{2TK^2}$

Speckle Flow Index

8000
6000
4000
2000

Fig. 2. Data flow. Left: Optical properties are calculated from a single raw image of data. The image is Fourier transformed line-by-line then window-filtered in frequency space. Component spectra are inverse-transformed and calibrated to phantom data to produce DC and AC images. Calibrated data are used to calculate μ_a and μ_s'. Right: Speckle flow index is calculated from the same raw image. A sliding window filter is used to compute the spatial standard deviation and mean intensity. The ratio of these quantities produces the speckle contrast (K) image. Speckle Flow Index (SFI) is then calculated from speckle contrast according to the equation above where T is the integration time.

Flow-phantom experiments

A wide-field flow phantom (Fig. 4) was constructed and used to validate single snapshot cSFDI. More specifically, this experiment was used to evaluate the sensitivity of this technique to changes in flow compared to conventional LSI. The phantom was constructed out of silicone using India ink as the absorbing agent and titanium dioxide as the scattering agent. A 13 mm x 13 mm square acrylic tube was embedded during the curing process to act as a flow channel. The wall thickness of the acrylic was 1.7 mm and the proximal surface of the tube was less than 500 µm beneath the surface of the silicone. The plastic tube was coupled to a syringe pump (New Era Pump Systems) to precisely control the flow speed. During the experiment, the phantom was imaged using both single snapshot cSFDI and conventional LSI while varying the speed of 1% Intralipid from 1 to 5 mm/s in 1 mm/s increments. This range was chosen to reflect red blood cell velocities encountered in

microcirculation [25]. Conventional LSI was performed by projecting planar coherent illumination, while single snapshot cSFDI was performed by projecting spatially modulated coherent illumination. In every other way (aperture, exposure time, optics) the two measurements were completely identical. Fifty sequential frames were acquired at each flow speed. SFI maps were calculated for each frame and averaged over a region of interest that was positioned over the entire length of the tube. Additionally, μ_a and μ_s' maps were recovered from one of the single snapshot cSFDI data sets to demonstrate its ability to recover spatial maps of all three sources of optical contrast.

Forearm reactive hyperemia experiment

An imaging study was performed on the forearm of a healthy subject undergoing a standard reactive hyperemia protocol. During this protocol an automatic inflatable cuff was wrapped around the subject's left upper arm. A full arterial occlusion was applied by inflating the cuff to 210 mmHg. During the imaging study, the volar forearm was imaged at 50 frames per second for 1 minute of baseline, followed by 3 minutes of arterial occlusion, followed by 3 minutes immediately after the release of the occlusion. Each of the 21,000 frames of data was used to reconstruct 2D maps of μ_a, μ_s', and SFI. Regions of interest were analyzed to obtain time course data of μ_a, μ_s' and SFI. Studies here were carried out under the UC Irvine IRB approved protocol, and informed consent was obtained from all subjects (HS# 2011-8370).

Results

Homogeneous phantom experiments

Figure 3 shows the results of the homogeneous phantom experiments comparing the optical properties recovered with single snapshot cSFDI and conventional SFDI. The graph at the bottom-left of Fig. 3 shows absorption recovered with single snapshot cSFDI plotted against absorption recovered using conventional SFDI. Each point corresponds to a different homogeneous phantom with unique optical properties. The blue horizontal lines are the standard deviation over the region of interest using SFDI, while the red vertical lines are the standard deviation using single snapshot cSFDI. Each error bar in Fig. 3 is calculated from a single reconstructed image and represents the spatial standard deviation over a 10 cm x 10 cm region of interest as described in Cuccia et al. and Vervandier et al. [14, 21]. The diagonal dashed line is a reference line representing perfect agreement between the two techniques. The average percent difference in μ_a between the two methods was less than 1.2%. On average, the standard deviation of μ_a over the region of interest using SFDI was 0.00083 mm^{-1} while the standard deviation using single snapshot cSFDI was 0.0013 mm^{-1}. The bottom right of Fig. 3 shows the comparison between bulk μ_s' reconstructed using both methods. Again, each of the points corresponds to a different phantom with unique μ_s'. Due to overlap in μ_s' of some of the phantoms, only five points are shown. The average percent difference between the two methods was 0.59%. The average standard deviation in μ_s' was 0.033 and 0.045 mm^{-1} for conventional SFDI and single snapshot cSFDI, respectively. Overall, these plots of μ_a and μ_s' demonstrate very good agreement in bulk optical property recovery. The images along the top are the reconstructed optical property maps recovered from one of the phantoms using conventional SFDI and single snapshot cSFDI.
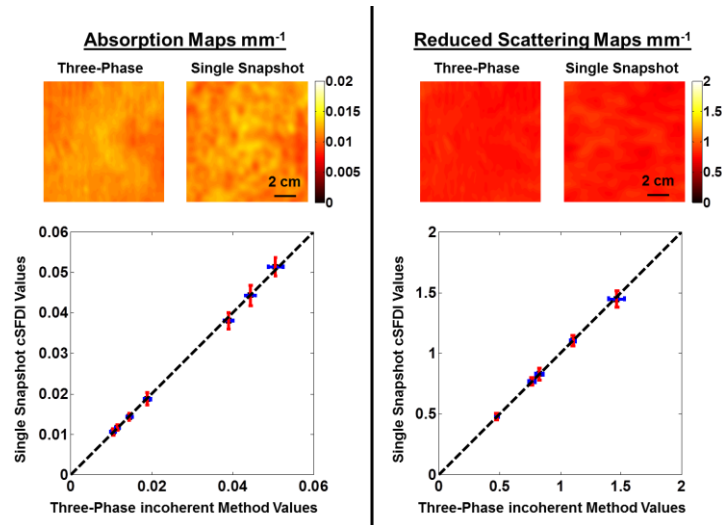
Fig. 3. Bulk optical property measurements. Left: comparison of bulk absorption reconstruction using standard three-phase SFDI and single snapshot cSFDI. Top two images show absorption maps reconstructed from one phantom using SFDI and single snapshot cSFDI. The bottom plot shows a comparison of bulk absorption between SFDI and single snapshot cSFDI calculated from seven different phantoms. Right: comparison of bulk reduced-scattering reconstruction. The top two images show reduced-scattering maps reconstructed using SFDI and single snapshot cSFDI. The plot at the bottom shows a comparison of bulk reduced-scattering between SFDI and single snapshot cSFDI calculated from five different phantoms.

Flow phantom experiment

Figure 4 shows a comparison between SFI recovered using modulated AC illumination (single snapshot cSFDI) and planar DC illumination (conventional LSI). Figure 4(A) contains snapshot SFI images of the phantom demonstrating comparable image quality using both methods. Figure 4(B) presents the comparison between SFI recovered with AC (single snapshot cSFDI) and DC (conventional LSI) projections over the area of flow as speed is increased from 1 to 5 mm/s. Each point corresponds to the SFI at a unique flow speed. These measurements were calculated by averaging over 50 frames of SFI maps. The red error bars represent the standard deviation over the 50 frames calculated from the AC projections while the blue error bars are the standard deviation using DC projections. The dashed line is a trend line fit to these points demonstrating a linear relationship among them. Unlike Fig. 3, this line is not a "y = x" reference line.
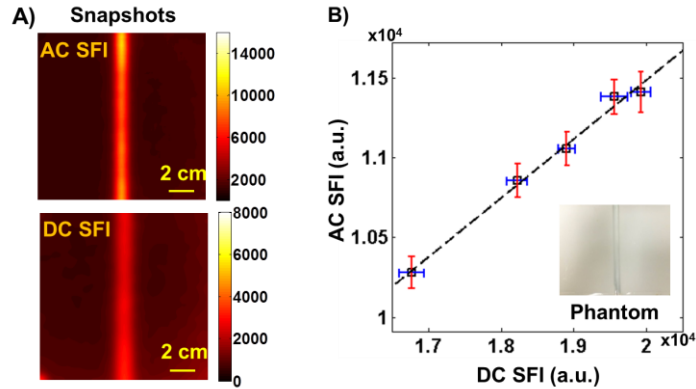
Fig. 4. SFI measurements. A) SFI images obtained from a flow phantom using spatially modulated AC projections (top) and planar DC projections (bottom). B) SFI values averaged over the region of flow as the speed of the moving liquid is increased from 1 to 5 mm/s in 1 mm/s increments. The graph shows SFI from AC illumination plotted against SFI from DC illumination at each flow speed.

Forearm reactive hyperemia experiment

Figure 5 shows the results from the reactive hyperemia experiment. The images across the top of the figure from left to right are the reconstructed μ_a, μ_s', and SFI maps. The plots along the bottom from left to right are the time-series data for μ_a, μ_s', and SFI. The red and blue curves in the time-series data are derived from the correspondingly-colored red and blue regions of interest (ROI) overlaid on the property maps. Both ROIs were chosen by visually assessing the absorption image in Fig. 5. The blue ROI was placed over an area with a subcutaneous vein, while the red ROI was placed over an area without one. The time-series data also indicate when the occlusion and release of the pressure cuff occurred. During the occlusion, there was a 32% increase in absorption in the blue channel and a 71% increase in the red ROI. These increases in μ_a were gradual and corresponded primarily to the accumulation of deoxyhemoglobin during the occlusion. Following the release there was a 43% decrease in μ_a in the blue ROI and a 72% decrease in the red ROI. This decrease occurred in less than 25 seconds and was caused by the reperfusion of oxyhemoglobin and the washout of deoxyhemoglobin. SFI showed a decrease of 51% in the red ROI and 28% in the blue ROI during the occlusion. After the release, there was a 190% increase in the red ROI and a 146% increase in the blue ROI. These large increases occurred over the course of 10 seconds indicating the immediate return of flow to the forearm. Changes in μ_s' are also seen during the occlusion and release portion of the experiment. However, these variations were significantly smaller than those witnessed in μ_a and SFI. Elucidating the nature and significance of these slight variations is left to future studies.

Absorption (mm⁻¹)   **Reduced Scattering (mm⁻¹)**   **SFI (a.u.)**

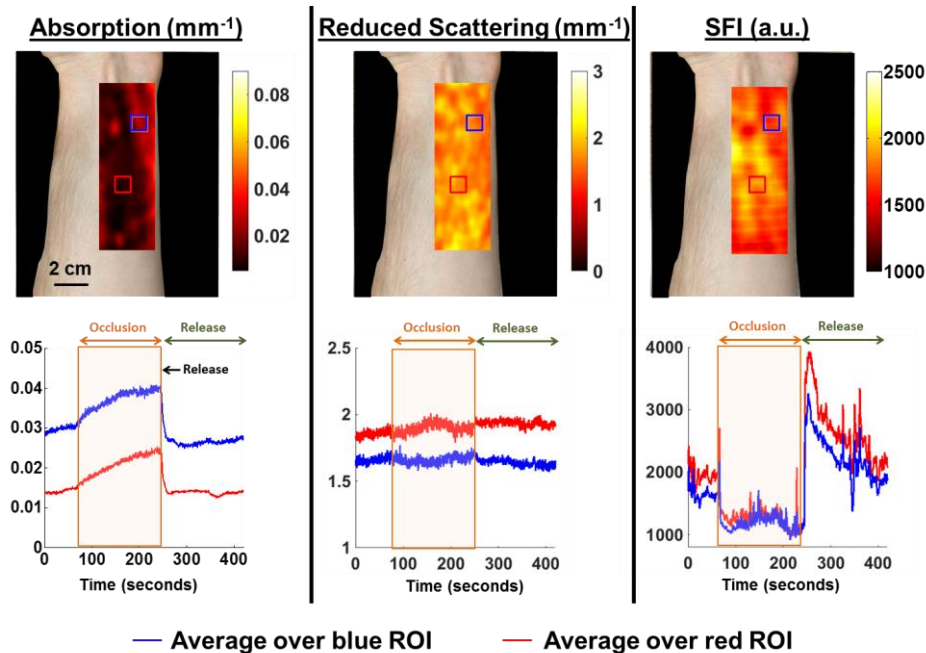— Average over blue ROI   — Average over red ROI

Fig. 5. *In vivo* forearm reactive hyperemia experiment. Top from left to right: spatial maps of absorption, reduced-scattering, and speckle flow index. Bottom from left to right: time-series data of absorption, reduced-scattering and speckle flow index from the two regions of interest in the images. A 660 nm laser diode was used in this experiment.

Figure 6 demonstrates the ability of single snapshot cSFDI to detect the heartbeat waveform within the SFI at multiple regions of interest within the field of view. Figure 6(a) shows one frame from the recovered SFI map overlaid on the subject's forearm during the reactive hyperemia protocol. The black and blue regions of interest correspond to the black and blue time-series data within the rest of Fig. 6. Figure 6(b) shows the entire cuff-occlusion-release time-series data. The brown shaded region lies over the occlusion segment while the green shaded region lies over the release of the occlusion. These data both demonstrate sensitivity to reactive hyperemia signified by the increase in SFI following the occlusion. Figure 6(c) shows the frequency spectrum of the blue curve in Fig. 6(b) for the segment during the occlusion (brown box) and the release (green box). The peak in the release at 1.2 Hz corresponds to the heartbeat signal (72 beats per minute). These spectra demonstrate the presence of the heartbeat component during the release that is absent during the occlusion due to the upstream arterial blockade of blood flow. This is confirmed intuitively by Fig. 6(d) which shows zoomed-in plots of both curves during 30 seconds of the occlusion and 30 seconds of the release. Note the periodic signal that is present during the release. Upon close inspection it is apparent that these two curves (black and blue) are both of the same frequency and phase over the entire duration. In contrast the segment from the occlusion data is more chaotic and lacks a clear periodic signal. Finally, Fig. 6(e) shows an even more zoomed-in view of the release segment, revealing a more detailed look at the heartbeat. Here it is possible to see structure within the signal during each heartbeat. These features could possibly contain information about the vasculature such as the dicrotic notch and reflections within the arterial tree. The spacing of the peaks was analyzed and shown to be at 1.2 Hz, in agreement with the Fourier analysis.
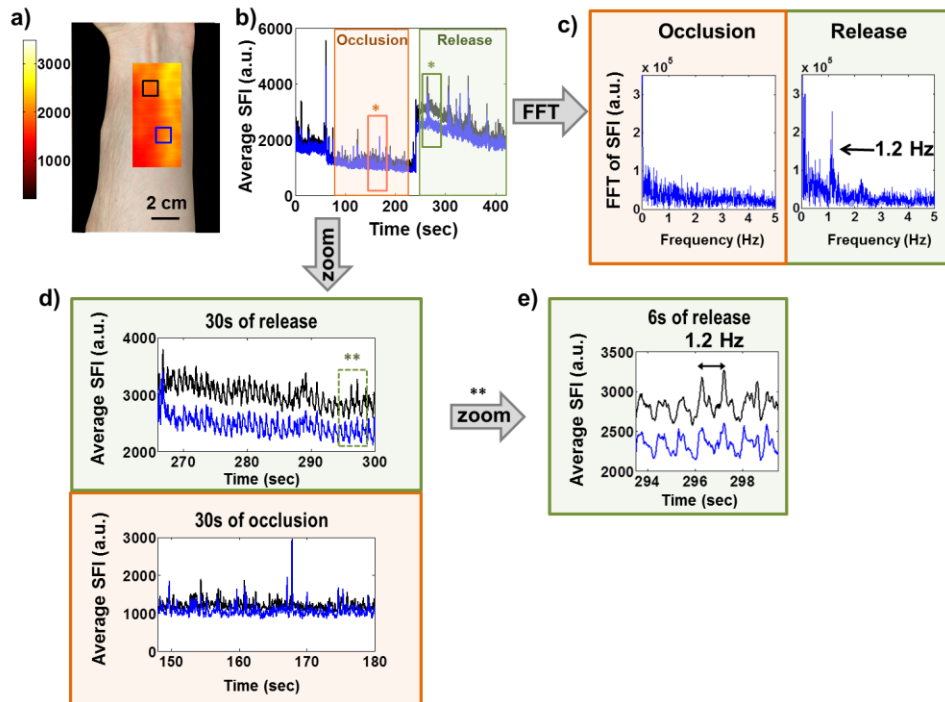
Fig. 6. Heartbeat data from *in vivo* experiments a) Image of the subject's forearm with overlaid SFI map. b) Time series SFI data from blue and black regions of interest during the cuff-occlusion-release protocol. The light-brown shaded box corresponds to the occlusion portion of the experiment, while the light-green shaded box corresponds to the release of the occlusion. c) Fourier transforms from the occlusion (light-brown) and the release (light-green). d) 30 second zoomed-in intervals taken from the occlusion and release portions of the data. The green shaded box corresponds to the green rectangle with the asterisk in Fig. 6(b). The brown shaded box is a zoomed in interval from the brown rectangle with the asterisk in Fig. 6(b). e) An even closer look at the signal during the release. These data correspond to the green rectangle with two asterisks (**) in Fig. 6(d).

Discussion

In this work we introduce a noncontact noninvasive imaging technique capable of extracting μ_a, μ_s', and SFI in real-time (50 fps) over large (15 x 15 cm) tissue regions. By applying advanced processing techniques to single raw images of spatially modulated coherent light, we are able to calculate optical properties from a single frame of data. Additionally, speckle contrast can be extracted from the same image because of its coherent properties. Needing only a single frame of data allows for simplified hardware; a fixed object such as a sinusoidal-patterned slide can be used in place of a DMD or LCOS projector in the case of conventional SFDI.

Homogeneous phantom experiments demonstrate that single snapshot cSFDI can be used to recover accurate optical properties over large ranges of absorption and reduced-scattering when compared with conventional 3-phase SFDI using an incoherent light source. Flow phantom experiments show that single snapshot cSFDI has comparable sensitivity to LSI in terms of measuring dynamic scatterer flow speeds. These same experiments also demonstrate the ability of single snapshot cSFDI to extract all three contrast mechanisms from a single frame of raw data. Access to this information enables the correction of speckle contrast for optical properties. In addition, an advantage to calculating speckle contrast from an AC projection is that it is possible to achieve higher speckle contrast values by rejecting long path-length photons [5, 6]. This is why in Fig. 4 the SFI is lower for the AC modulation

pattern; SFI is inversely proportional to speckle contrast, and speckle contrast from an AC projection is higher than the corresponding DC illumination. This potentially enables more accurate characterization of superficial microcirculation.

In vivo studies of reactive hyperemia demonstrate the ability of single snapshot cSFDI to measure intrinsic signals relevant to dynamic physiology. During the occlusion we observed increases in μ_a at 660 nm indicative of a buildup of deoxyhemoglobin. Following the release of the occlusion we observe a sharp decrease in μ_a signifying the washout of deoxyhemoglobin as oxyhemoglobin re-entered the tissue compartment. The increase in SFI above baseline observed after the occlusion demonstrates sensitivity to post occlusive reactive hyperemia, a well-established physiological phenomenon.

Beyond demonstrating sensitivity to dynamic physiological processes, these *in vivo* measurements point to the potential of single snapshot cSFDI to measure the tissue metabolic rate of oxygen consumption. The current system presented in this paper has only a single optical wavelength, and is therefore only capable of extracting tissue absorption and scattering coefficients. However, by extending this system to multiple wavelengths it would have the ability to decouple the chromophore concentrations of oxy- and deoxyhemoglobin ([HbO$_2$] and [HHb], respectively). Combining blood hemoglobin concentrations with flow measurements can be used to generate an index for oxygen consumption in accordance with Fick's principle. Measuring the metabolic rate of oxygen consumption has multiple potential applications and can provide important insight into pathologic conditions where flow and metabolism are uncoupled. For example, oxygen utilization is known to be decreased in conditions of chronic hypoxia caused by prolonged arterial occlusion, such as peripheral arterial disease (PAD). Real-time measurements could provide clinicians with important information relevant to early diagnosis, disease staging, and treatment response monitoring.

The ability to extract spatial maps of multiple contrast sources in real-time has numerous potential benefits outside of oxygen metabolism. In this work we were able to observe the heartbeat in the SFI channel. Characterization of the heartbeat waveform has potential to unlock information related to arterial stiffness and blood pressure [26, 27]. By observing the heartbeat over large tissue areas it may be possible to directly observe pulse transit time by measuring how the waveform changes in phase over areas of tissue. In this work we performed imaging using a 660 nm laser diode, a wavelength with greater sensitivity to deoxyhemoglobin than oxyhemoglobin. By performing single snapshot cSFDI with a wavelength with greater HbO$_2$ sensitivity (e.g. 850 nm) there is potential to measure the plethysmographic waveform in the absorption or DC reflectance data. In this case, single snapshot cSFDI would be able to measure the heartbeat simultaneously in absorption and SFI, and potentially be used to look at shifts in phase associated with intrinsic physiology.

Beyond physiology, mapping multiple contrast sources has the potential to improve quantitative accuracy of SFI. Previous work has demonstrated that speckle contrast is dependent on tissue optical properties and the sampling volume. Changes in the absorption and reduced scattering coefficients were shown to change speckle contrast for a given flow speed. Likewise, the depth at which flow occurs also affects the speckle contrast recovered at a given flow speed. Single snapshot cSFDI has the ability to correct for both of these effects. An optical property alteration algorithm, based on Monte-Carlo simulations of light transport, can take into account the optical properties recovered using single snapshot cSFDI to adjust the speckle contrast, and thus SFI values. Additionally, speckle contrast calculated in the spatial frequency domain can be used to control for the measurement depth. Together, these effects can be used to improve quantitative accuracy of the speckle contrast measurements in single snapshot cSFDI [5, 6].

In summary the information rich spatiotemporal data set recovered by single snapshot cSFDI has significant potential. By combining blood concentrations with blood flow speed there is the possibility to measure chromophore concentrations. Measuring the heartbeat in the absorption parameter and speckle contrast channels may reveal physiologically relevant

information about microcirculatory physiology. Finally, single snapshot cSFDI offers the potential to improve quantitative accuracy of speckle information by controlling for optical properties and measurement volume. In future work, this system will be extended to multiple wavelengths to measure chromophores then transformed into a portable clinic-ready device suitable for *in vivo* physiological measurements.

Acknowledgments

Conflict of Interest

The authors (B.J.T., A.J.D) have received or will receive benefits for personal or professional use from commercial parties related directly or indirectly to the subject of the manuscript.